

The representation of finger movement and force in human motor and premotor cortices

<https://doi.org/10.1523/ENEURO.0063-20.2020>

Cite as: eNeuro 2020; 10.1523/ENEURO.0063-20.2020

Received: 19 February 2020

Revised: 6 May 2020

Accepted: 21 May 2020

This Early Release article has been peer-reviewed and accepted, but has not been through the composition and copyediting processes. The final version may differ slightly in style or formatting and will contain links to any extended data.

Alerts: Sign up at www.eneuro.org/alerts to receive customized email alerts when the fully formatted version of this article is published.

Copyright © 2020 Flint et al.

This is an open-access article distributed under the terms of the Creative Commons Attribution 4.0 International license, which permits unrestricted use, distribution and reproduction in any medium provided that the original work is properly attributed.

1 1. **Manuscript Title: The representation of finger movement and force in human**

2 **motor and premotor cortices**

3 2. Abbreviated title: Finger movement and force in human M1 and PM

4 3. Author names and affiliation: Robert D. Flint^{*1,2}, Matthew C. Tate^{1,3}, Kejun Li⁴,

5 Jessica W. Templer¹, Joshua M. Rosenow^{1,3,5}, Chethan Pandarinath^{6,7,8}, Marc W.

6 Slutzky^{1,2,5,9,10}

7 ¹Department of Neurology, Northwestern University, Chicago IL 60611, USA,

8 ²Shirley Ryan AbilityLab, Northwestern University, Chicago IL 60611, USA,

9 ³Department of Neurological Surgery, Northwestern University, Chicago IL 60611,
10 USA, ⁴Computation and Neural Systems Program, California Institute of Technology,

11 Pasadena, California 91125, USA, ⁵Department of Physical Medicine &

12 Rehabilitation, Northwestern University, Chicago IL 60611, USA, ⁶Department of

13 Biomedical Engineering, Emory University and Georgia Institute of Technology,

14 Atlanta GA 30322, USA, ⁷Department of Neurosurgery, Emory University, Atlanta

15 GA 30322, USA, ⁸Emory Neuromodulation and Technology Innovation Center

16 (ENTICE), Emory University, Atlanta GA 30322, USA, ⁹Department of Physiology,

17 Northwestern University, Chicago IL 60611, USA. ¹⁰Department of Biomedical

18 Engineering, Northwestern University, Chicago IL 60611, USA

19 4. Author contributions: RDF and MWS designed research; RDF, MCT, JWT, JMR,

20 and MWS performed research; RDF, KL, CP, and MWS analyzed data; RDF, KL,

21 CP, and MWS wrote the paper.

22

23

- 24 5. Correspondence should be addressed to:
25 Robert D Flint
26 Research Assistant Professor, Neurology
27 Feinberg School of Medicine
28 Northwestern University
29 r-flint@northwestern.edu
- 30 6. Number of Figures: 6
- 31 7. Number of Tables: 2
- 32 8. Number of Multimedia: 0
- 33 9. Number of words for Abstract: 200
- 34 10. Number of words for Significance Statement: 117
- 35 11. Number of words for Introduction: 650
- 36 12. Number of words for Discussion: 1946
- 37 13. Acknowledgements: This work was supported by the following sources: Craig H
38 Neilsen Foundation fellowship (RDF); Emory College Computational
39 Neuroscience training grant (KL); Burroughs Wellcome Fund Collaborative
40 Research Travel Grant (CP); National Science Foundation NCS 1835364 (CP);
41 Emory Neuromodulation Technology Innovation Center (CP); Doris Duke
42 Charitable Foundation Clinical Scientist Development Award (MWS);
43 Northwestern Memorial Foundation Dixon Translational Research Grant
44 Program (supported in part by NIH Grant UL1RR025741) (MWS); National
45 Institutes of Health R01NS094748 (MWS). We would like to thank our research
46 subjects for their participation, and Mukta Vaidya for helpful comments on the

47 manuscript.

48 14. Conflict of Interest: Authors report no conflict of interest

49

50

51 **Abstract**

52 The ability to grasp and manipulate objects requires controlling both finger
53 movement kinematics and isometric force in rapid succession. Previous work suggests
54 that these behavioral modes are controlled separately, but it is unknown whether the
55 cerebral cortex represents them differently. Here, we asked the question of how
56 movement and force were represented cortically, when executed sequentially with the
57 same finger. We recorded high-density electrocorticography (ECoG) from the motor and
58 premotor cortices of seven human subjects performing a movement-force motor task.
59 We decoded finger movement (0.7 ± 0.3 fractional variance accounted for; FVAF) and
60 force (0.7 ± 0.2 FVAF) with high accuracy, yet found different spatial representations. In
61 addition, we used a state-of-the-art deep learning method to uncover smooth, repeatable
62 trajectories through ECoG state space during the movement-force task. We also
63 summarized ECoG across trials and participants by developing a new metric, the neural
64 vector angle. Thus, state-space techniques can help to investigate broad cortical
65 networks. Finally, we were able to classify the behavioral mode from neural signals with
66 high accuracy ($90 \pm 6\%$). Thus, finger movement and force appear to have distinct
67 representations in motor/premotor cortices. These results inform our understanding of
68 the neural control of movement, as well as the design of grasp brain-machine interfaces.
69

70 **Significance Statement**

71 The human ability to manipulate objects is central to our daily lives and requires
72 control of both grasping movement and force. Here, we explored how these motor
73 activities are represented at the level of the cortex. Understanding these representations
74 will influence the design of brain-machine interfaces (BMIs) to restore function after
75 paralysis. We recorded electrocorticography (ECoG) from seven human subjects who
76 performed a sequential movement-force motor task. We found differences between the
77 cortical representations of movement and force using decoding methods, deep learning,
78 and a new neural ensemble metric. Thus, ECoG could be used in a BMI to control both
79 movement and force behaviors. These results can potentially accelerate the translation of
80 BMIs for individuals with paralysis.

81

82

83 **Introduction**

84 The human ability to grasp and manipulate objects is central to our evolutionary
85 success as tool users. The loss of this ability has a profound negative impact on overall
86 quality of life. We rely in particular upon our ability to precisely regulate movement and
87 force, to close our fingers around an object, then exert isometric force sufficient to
88 prevent slippage without crushing it. However, the neural origin of this process is not yet
89 clear. In the current study, we sought to identify how movement and force are encoded at
90 the cortical level when both are performed sequentially.

91 There is longstanding evidence for cortical representations of both movement
92 (Moran and Schwartz, 1999) and force (Evarts, 1968). There is also indirect evidence
93 that distinct neural control states are used for kinematics (movement) and kinetics (force).
94 For example, motor learning of kinematics and kinetics in reaching occur independently
95 of each other (Flanagan et al., 1999). Kinematic and kinetic control can be disrupted
96 independently (Chib et al., 2009), and their errors can be separated during adaptation
97 (Danion et al., 2013). Perhaps most relevant, Venkadesan and Valero-Cuevas (2008),
98 found that electromyogram (EMG) activity patterns transitioned between separate,
99 incompatible states during a one-finger, sequential movement-force task. Importantly,
100 these transitions occurred prior to the fingertip's contact with a surface, implying that
101 changing neural states may "prepare" finger muscle activations for their upcoming role in
102 regulating force. Here, we hypothesized that the transition between movement and force
103 is encoded in motor and premotor cortical networks.

104 The specifics of cortical movement and force encoding are also relevant to brain-
105 machine interface (BMI) design (Downey et al., 2018; Branco et al., 2019a; Slutzky,

2019; Rastogi et al., 2020). Restoration of hand grasp functionality is a high priority for individuals with paralysis (Blabe et al., 2015). Currently, BMIs using motor cortical signals control robotic or prosthetic hands (Hochberg et al., 2012; Yanagisawa et al., 2012; Wodlinger et al., 2014; Hotson et al., 2016), or functional electrical stimulation of paralyzed limbs (Pfurtscheller et al., 2003; Bouton et al., 2016; Ajiboye et al., 2017). However, most BMIs that have decoded grasp intent have focused on decoding kinematics of grasp aperture. One exception improved BMI-prosthetic hand control by scaling the neuronal firing rates (Downey et al., 2017), but did not examine the movement-force transition. Here, we hypothesized that force and kinematics of the hand are governed by different neural states in cortex.

In the current study, we used a sequential movement-force task to investigate changes in human cortical activity during transitions in behavioral mode: from pre-movement (preparation) to movement to force. We recorded subdural surface potentials (electrocorticography; ECoG), finger kinematics, and applied force. We used ECoG spectral modulations to measure changes in the spatial patterns of movement- and force-based decoding, and to classify the behavioral mode of the subject. We found evidence of distinct movement and force encoding.

Recent work has characterized changes in cortical network activity during kinematic tasks as the temporal evolution of a dynamical system (Churchland et al., 2012; Pandarinath et al., 2018). Here, we examined whether neural state space changes accompanied behavioral mode transitions (from pre-movement to movement to force). We used latent factor analysis via dynamical systems (LFADS), a deep-learning method that uses sequential autoencoders to uncover trajectories in a low-dimensional neural

129 state space from high-dimensional neural data (Pandarinath et al., 2018). We also
130 calculated changes in a neural vector angle (NVA), obtained by treating the spectral
131 features as elements of a high-dimensional neural vector. Both approaches showed that
132 activity across a broad area of motor and premotor cortices exhibited tightly clustered
133 trajectories through neural state space that were time-locked to the behavior. The NVA
134 enabled us to average responses across subjects and create a generalized temporal profile
135 of neural state space activity during the movement and force modes of human grasp.
136 Together, these analyses indicate that distinct cortical states correspond to the distinct
137 movement and force modes of grasp.

138

139 **Materials and Methods**

140 **Subjects and recordings**

141 Seven human subjects participated in the study (all male; ages 26-60, ordered
142 chronologically). Six of the subjects required awake intraoperative mapping prior to
143 resection of low-grade gliomas. Their tumors were located remotely to the cortical areas
144 related to hand grasp, and no upper extremity sensorimotor deficits were observed in
145 neurological testing. Subject S6 underwent extraoperative intracranial monitoring prior
146 to resection surgery for treatment of medication-refractory epilepsy. All human subjects
147 were recruited at Northwestern University. The experiments were performed under
148 protocols approved by the institutional review board. All subjects gave written informed
149 consent before participating in the study. Subjects were recruited for the study if the site
150 of their craniotomy, or their monitoring array was expected to include coverage of
151 primary motor cortex.

152 In all subjects except S6, we used 64 electrode (8x8) high-density ECoG arrays,
 153 with 1.5-mm exposed recording site diameter and 4-mm inter-electrode spacing (Integra,
 154 Inc.). Arrays were placed over hand motor areas, which we defined by: 1) anatomical
 155 landmarks, e.g., ‘hand knob’ in primary motor cortex; 2) pre-operative fMRI or
 156 transcranial magnetic stimulation to identify functional motor areas; and 3) direct
 157 electrocortical stimulation mapping. Intraoperative recordings took place after direct
 158 stimulation mapping. Intraoperative MRI navigation was performed with Curve
 159 (BrainLab, Inc., Munich, Germany). The recording arrays covered primary motor cortex,
 160 premotor cortex, and usually part of primary somatosensory cortex as well (Figure 1A).
 161 In S6, electrode placement was determined by clinical need. For this subject, we used a
 162 32-electrode (8x4) array with the same electrode size and spacing as our 64-electrode
 163 arrays.

164 We sampled ECoG at 2 kHz using a Neuroport Neural Signal Processor
 165 (Blackrock Microsystems, Inc.). Signals were bandpass filtered between 0.3 Hz and 500
 166 Hz prior to sampling. Finger kinematics were recorded using a 22-sensor CyberGlove
 167 (Immersion). We recorded force with a custom-built load cell sensor. Kinematic and
 168 kinetic data were both sampled at the same rate as ECoG.

169

170 **Experimental protocol**

171 The subjects executed repeated trials of a one-finger task that required isotonic movement
 172 and isometric force in sequence (Figure 1B). At the beginning of each trial, the subjects
 173 were instructed to hold their index finger in a neutral posture (the “pre-movement”
 174 behavioral mode). After a cue, they executed a self-paced flexion movement, which

175 brought the palmar surface of the index finger into contact with the force sensor. Upon
176 contact, subjects were instructed to apply force to the sensor, thereby controlling a cursor
177 on a monitor. Their task was to match the cursor's vertical position to that of a force
178 target presented on the monitor. Target force levels varied randomly from trial to trial
179 (random-target pursuit task). Following a successful match (or a timeout of 2s), the trial
180 was complete, and the subject extended their finger back to the baseline (neutral)
181 position. The next trial began after a delay of 1s. Target presentation and cursor
182 feedback were carried out by the open-source BCI2000 software (Schalk et al., 2004).
183 The time resolution for both kinematic data acquisition and force cursor control was
184 50ms.

185 Our task was designed to elicit movement by, and force using one finger, keeping
186 the other fingers motionless in a flexed position. Therefore, our kinematic data consisted
187 of the CyberGlove sensors that measured the motion of the index finger (Figure 1C,
188 highlighted). Dominant kinematic features were extracted via principal component
189 analysis (PCA). We performed PCA only on data from the highlighted sensors in Figure
190 1C, retaining the 1st component to identify movement onset (the cyan trace in Figure 1B
191 shows an example of the movement signal we used).

192

193 **Feature extraction**

194 For all analyses, we extracted spectral features from each ECoG electrode. Here,
195 each feature was the mean spectral power in a frequency band of interest. The sampling
196 rate was 2000 Hz. To compute spectral power, we applied a Hanning window function to
197 256-ms segments of data, followed by a Fourier transform. We normalized the log of this

198 power by subtracting the log of the mean power over the entire file, then extracted
 199 spectral features by averaging within frequency bands of interest (see below). The
 200 resolution of the frequency axis was 3.9 Hz. Each data segment (or time bin, to borrow
 201 nomenclature from past single-neuron studies) overlapped the previous by 231 ms, giving
 202 the analysis an effective temporal resolution of 25 ms.

203 We identified the feature boundaries (frequency bands of interest) by computing
 204 the event-related spectral perturbation (ERSP) for each electrode around the time of force
 205 onset. We then averaged the ERSPs for all electrodes in our dataset, and identified the
 206 frequency bands of interest: broadband low frequency (8-55 Hz) and broadband high
 207 frequency (70-150 Hz). Subsequent analyses were performed on the feature matrix for
 208 each subject. Each feature matrix was size $N \times M$, where N is the number of time bins in
 209 the record, and M is $2 \times (\text{number of electrodes}) \times 10$, where 10 was the number of time bins
 210 into the past (causal bins only).

211

212 **Population decoding of continuous movement and force**

213 We decoded continuous movement kinematics and continuous isometric force,
 214 using all (non-noisy) electrodes from PM and M1 in each subject. For continuous
 215 decoding, the feature matrix served as input to a Wiener cascade decoder (Hunter and
 216 Korenberg, 1986). In the Wiener cascade, the output of a linear Wiener filter is
 217 convolved with a static nonlinearity (here, a 3rd-order polynomial). We employed ridge
 218 regression to reduce the likelihood of overfitting due to the large feature space, as in
 219 (Suminski et al., 2010). We evaluated decoding accuracy using the fraction of variance
 220 accounted for (FVAF). We employed 11-fold cross-validation, using 9 folds for training,

221 1 fold for parameter validation (e.g., optimizing the free parameter in the ridge
222 regression; Fagg et al., 2009), and 1 fold for testing. We report the median \pm interquartile
223 range (IQR) of FVAF across test folds. Movement and force were treated as separate,
224 independent sources of information for continuous decoding. All sampled times were
225 used to decode movement, whether the subject was in pre-movement, movement, force,
226 or between trials. Likewise, all sampled times were used to decode force. The purpose
227 of decoding continuous movement and force was to validate the information content of
228 the ECoG signals. Thus, a high FVAF indicated that the ECoG signals encode
229 information about times of active behavior (movement or force) as well as rest periods,
230 and transitions among behavioral modes.

231

232 **Spatial mapping of decoding performance**

233 We quantified the difference in the spatial representations of movement and force
234 using two measures: (1) change in location of the peak single-electrode decoding
235 performance, and (2) change in the overall spatial distribution of single-electrode
236 decoding performance. For both analyses, we decoded continuous movement for each
237 individual ECoG electrode using Wiener cascade decoders, as in the previous section. As
238 above, all data (regardless of behavioral mode) were used to evaluate decoding accuracy
239 using the cross-validated FVAF. The spatial distribution of single-electrode movement
240 decoding performance formed a “map” for the array. In a similar manner, we constructed
241 a “map” of force decoding performance. We then analyzed these maps to reveal
242 differences between movement and force spatial representation patterns on the cortical
243 surface.

244 We compared the location of the overall peak of each decoding map for
 245 movement to that of force within each cross-validation fold. We report the absolute
 246 displacement between the peak performance location from force decoding vs. that from
 247 movement decoding. Peak performance displacement quantifies the shift in location
 248 between movement and force in units of distance (here, in millimeters).

249 In addition, we compared the overall decoding map patterns. The map for a
 250 single fold can be treated as an image, with FVAF values corresponding to pixel
 251 intensities. We measured similarity among maps using a differencing metric common to
 252 image processing (Euclidean distance). We calculated the distance (D) between pairs of
 253 maps for individual folds. For example, a value of $D_{\text{intra},3-4(\text{force})}=0$, where D is the
 254 difference metric, would indicate that the force decoding maps in folds 3 and 4 were
 255 identical. We compared the inter-map distances across behavioral modes (movement vs.
 256 force, D_{inter}) to find the average decoding map difference between movement and force
 257 encoding on the cortex. We compared these to within-modality distances
 258 ($D_{\text{intra}(\text{force})}, D_{\text{intra}(\text{mvt})}$), which vary only due to time. That is, D_{intra} measured map
 259 differences within a behavioral mode, which can be attributed to variance in task
 260 performance across trials. Thus, D_{intra} values served as controls for D_{inter} , which
 261 measured the map differences attributable to behavioral mode (movement or force).
 262 When calculating these distance metrics between performance maps, we scaled by the
 263 maximum possible distance between the maps, so that both D_{inter} and D_{intra} ranged from 0
 264 to 1.

265
 266

267

268 **Latent factor analysis via dynamical systems**

269 We used a deep learning algorithm known as latent factor analysis via dynamical
 270 systems (LFADS) to denoise ECoG features (Sussillo et al., 2016; Pandarinath et al.,
 271 2018). LFADS denoises neural activity based on the assumption that the observed
 272 patterns of neural modulation can be described as noisy observations of an underlying
 273 low-dimensional dynamical system. LFADS aims to extract a set of low-dimensional
 274 latent factors that describe neural population activity on a single-trial basis. When
 275 previously applied to spiking activity from populations of neurons, LFADS modeled
 276 observed spikes for each neuron as samples from an inhomogeneous Poisson process
 277 (called the firing rate), and attempted to infer this underlying firing rate for each neuron.
 278 In this study, since the ECoG features are continuous rather than discrete variables, the
 279 underlying distribution was taken to be Gaussian instead of Poisson. Specifically, the data
 280 was pre-processed by z-scoring each spectral feature. Then, the data was modeled
 281 following the equations in Sussillo et al. (2016), with the key modifications that:

$$282 \quad \mu_{r,t} = \mathbf{W}^{fac1}(\mathbf{f}_t) \quad (1)$$

$$283 \quad \sigma_{r,t} = \mathbf{W}^{fac2}(\mathbf{f}_t) \quad (2)$$

$$284 \quad x_t \sim N(\mu_{r,t}, \sigma_{r,t}^2), \quad (3)$$

285 where \mathbf{x}_t represents the vector of z-scored spectral features at each timestep, and \mathbf{f}_t
 286 represents the latent factors output by the LFADS recurrent neural network. For a given
 287 spectral feature r , $\mu_{r,t}$ and $\sigma_{r,t}$ represent the inferred time-varying mean and variance,
 288 respectively, for the z-scored spectral feature at each time step. \mathbf{W}^{fac1} and \mathbf{W}^{fac2} are

289 matrices that map the latent factors onto $\mu_{r,t}$ and $\sigma_{r,t}$, respectively. These matrices have
 290 fixed weights across all time points. For each subject, the number of latent factors
 291 allowed was approximately half the total number of ECoG channels used. After applying
 292 LFADS, we used principal component analysis to produce low-dimensional
 293 visualizations of the denoised ECoG features.

294 **Neural vector angle**

295 To compactly represent the overall response of a subject's feature set, we
 296 computed neural vector angles (NVAs) for each trial. This quantity is similar to the
 297 "muscle coordination pattern" angle of Venkadesan and Valero-Cuevas (2008). We
 298 selected features to include in the NVA calculations using the following method: first, we
 299 averaged the ECoG spectral intensity across trials, aligned to force onset. We then used
 300 unsupervised k-means clustering (3 clusters) to partition the trial-averaged spectral power
 301 from the complete set of features. All M1/PM features served as inputs to the clustering
 302 algorithm. We evaluated this algorithm with 2-5 input clusters in each subject, using
 303 silhouette values to judge the quality of clustering. Grouping the features into 3 clusters
 304 produced the best groupings (with zero negative silhouette values in most subjects). Of
 305 the three output clusters, we selected the two that were well-modulated with movement
 306 and/or force: a cluster of low-frequency features and a cluster of high-frequency features.
 307 These groupings for well-modulated features (low- and high-frequency) emerged natively
 308 from the unsupervised procedure, typically leaving one additional cluster of poorly-
 309 modulated features. Clustering was used only as a means of selecting ECoG features to
 310 include in NVA computations.

311 We calculated the NVA separately for the low- and high-frequency features, as
 312 follows: a cluster of features with n members can be represented at time t as
 313 $\mathbf{m}(t)=[f_1, f_2, \dots, f_n]$, where f is the value of an individual feature. We smoothed $\mathbf{m}(t)$ over 5
 314 time bins (total 125 ms), then calculated the neural vector angle

$$315 \quad \theta(t) = \cos^{-1} \left(\frac{\mathbf{m}(t) \langle \mathbf{m}^{ref} \rangle}{\|\mathbf{m}(t)\| \|\mathbf{m}^{ref}\|} \right) \quad (4)$$

316 where \mathbf{m}^{ref} is the average value of $\mathbf{m}(t)$ over the 250-ms period before the time of
 317 maximum force exertion in the trial. We computed the neural vector angle at each time
 318 bin over trials in each of the emergent clusters (low- and high-frequency modulating), for
 319 each subject. Since the neural vector angle transformed the data from feature values to a
 320 common coordinate system (angle between vectors, in degrees), it enabled us to average
 321 this quantity across subjects. To quantify differences in NVA values due to behavioral
 322 mode, we used the Kruskal-Wallis test of unequal medians on NVAs during “pre-
 323 movement”, “movement”, and “force” modes (illustrated in Figure 1B). See also the
 324 following section for details of the behavioral mode labelling procedure.

326 **Discrete classification of behavioral mode**

327 Our classification of behavioral mode utilized the same frequency-based features
 328 as we used in our continuous decoding analysis. Here, the data were selected and labeled
 329 as follows: time bins from target presentation to the start of finger flexion were labeled as
 330 “pre-movement”; time bins from the start of flexion to contact with the force sensor were
 331 labeled “movement”; time bins beginning at contact with the force sensor, continuing for
 332 0.5 s were labeled “force”. An example of this behavioral mode labelling for a single

trial of data is shown in Figure 1B. We limited the length of the force window to obtain more balanced class sizes. Data outside of the described time windows were discarded. The data were classified using two methods: support vector machines and boosted aggregate (bagged) trees. The classification analyses used 5-fold cross validation. Within each fold, we trained on (or tested) every individual 25-ms time bin. The reported accuracy measures are the median \pm IQR of correctly classified time bins across all test folds. Because the class sizes were not exactly equal, the chance level performance of the 3-class classifier was not necessarily 1/3. We calculated the true chance level performance by shuffling the class labels and then performing the analyses as above. We repeated this procedure 1000 times for each recording.

Experimental design and statistical analysis

We conducted the experiments and analyzed the data using a within-subject design. We used non-parametric statistics to report continuous kinematics and continuous force decoding accuracy, as the decoding accuracy values (FVAF) were distributed non-normally across cross-validation folds. To compare maps of decoding performance, we conducted a one-tailed Wilcoxon signed-rank test, with Bonferroni correction for multiple comparisons. Differences in NVA during behavioral modes were tested using a Kruskal-Wallis test. For the discrete decoding of behavioral mode, we also used a Kruskal-Wallis test to identify statistical differences between ECoG feature-based decoding and LFADS-cleaned feature decoding.

Results

356 We recorded ECoG from seven human subjects with brain tumors or epilepsy
357 who required intraoperative or extraoperative mapping as part of their clinical treatment.
358 In all subjects, ECoG coverage included at least part of primary motor and premotor
359 cortices (Brodmann areas 4 and 6). In some cases, coverage also included prefrontal
360 and/or postcentral cortices (Figure 1A). However, we restricted our analyses to
361 electrodes covering primary motor and premotor cortices. The subjects performed a cued
362 one-finger task requiring an isotonic flexion movement, followed by isometric flexion to
363 specified force targets. Movement and isometric flexion were performed sequentially
364 (Figure 1B). This task was adapted from Venkadesan and Valero-Cuevas (2008). We
365 recorded the finger joint kinematics (based on the sensors highlighted in Figure 1C) as
366 well as the force generated by isometric flexion.

367

368 **ECoG feature modulations were time-locked with movement and force**

369 Following Collard et al. (2016), we used event-aligned plots to visualize event-
370 related changes in ECoG spectral features, specifically to understand how tightly these
371 features modulated with behavioral events. We examined modulation with respect to (1)
372 the start of finger flexion movement and (2) the start of isometric force exertion. For
373 each feature, we constructed an “intensity raster” by windowing the feature’s data, then
374 plotting as trial number vs. peri-event time. We sorted trials by the elapsed time between
375 events.

376 We constructed intensity raster plots for each feature in our dataset (2 features per
377 non-noise electrode, 722 total features in the dataset). Overall, we found a diverse set of
378 activity patterns during movement and force production. Figure 2A shows an example of

eNeuro Accepted Manuscript

379 a high frequency feature that appears to encode both movement and force, showing
380 increased activity at the transition from pre-movement to movement (Figure 2A, left of
381 dashed line) and decreased activity after force onset (right of blue circles). Some high
382 frequency feature modulations were time-locked only to force execution (Figure 2B,C).
383 Examples of low frequency features exhibiting power decreases at movement onset are
384 shown in Figure 2D,E. Low-frequency power decrease could also be time-locked to the
385 start of force, instead (Figure 2F). Note that Figures 2B and 2E show high- and low-
386 frequency features from the same ECoG electrode, illustrating that two behavioral modes
387 can be encoded differently by high- and low-frequency information on the same
388 electrode. Overall, the results exemplified in Figure 2 indicate a heterogeneous set of
389 spectral feature responses to movement and force; in fact, we did not find a simple way to
390 combine feature intensity data that completely summarized the individual features'
391 responses across high- or low-frequency domains. Therefore, we also examined
392 population-level measures to obtain a more generalized description of how M1/PM
393 represents kinematic-kinetic behavior.

394
395 **Continuous movement and force were decoded with high accuracy using ECoG**

396 We used a Wiener cascade approach to build multi-input, single-output models
397 for decoding behavior. We built one such model to decode the continuous time course of
398 finger movement kinematics using both high and low spectral features from all (M1/PM)
399 electrodes. A separate model was built to decode continuous isometric force from the
400 same electrodes. Both movement and force were decoded at all times (not only during
401 active movement or active force) using a cross-validated design. The resulting decoding

402 accuracy was high for both force and kinematics: the fraction of variance accounted for
403 (FVAF) ranged from 0.4 ± 0.1 (median \pm IQR) to 0.8 ± 0.1 for the individual subjects.
404 Across subjects, the overall median FVAF was 0.7 ± 0.2 for force decoding, and 0.7 ± 0.3
405 for movement decoding. Statistically, the null hypothesis that movement kinematics and
406 force were decoded with equivalent accuracy could not be rejected (Kruskal-Wallis test,
407 $p=0.6$); thus, any differences between movement and force representations were not due
408 simply to decoding one quantity better than the other.

409

410 **Spatial mapping of decoding performance shows different cortical representations** 411 **of movement and force**

412 We next quantified the difference in the spatial representations of force and
413 movement on the cortical surface, using two metrics: (1) change in location of the peak
414 decoding performance electrode (Table 1), and (2) change in overall decoding map
415 pattern (Figure 3). A previous study found that decoding maps' peak performance
416 locations differed when two different fingers were used for an isometric force task (Flint
417 et al., 2014). Here, we found that the peak performance location was different for
418 movement and force decoding. The displacement (between movement and force) of the
419 peak decoding performance ranged from 3.2 ± 5.4 mm to 16.5 ± 8.8 mm across subjects
420 (mean \pm SD over folds; Table 1). The mean (\pm SE) displacement of peak performance for
421 all subjects was 9.9 ± 2.0 mm.

422

423

424

425

426

	mean	±	S.D.
S1	16.1	±	4.1
S2	16.5	±	8.8
S3	3.2	±	5.4
S4	10.2	±	8.4
S5	4.2	±	6.6
S6	8.8	±	5.4
S7	10.7	±	8.0

427 Table 1. Displacement of peak location (in mm) for movement decoding performance relative to

428 force decoding performance in each subject.

429 To place these distances in context, a standard ECoG array for epilepsy use has an inter-
 430 electrode distance of 10 mm, highlighting the advantages of using high-density ECoG
 431 arrays (the electrode arrays used here had an inter-electrode distance of 4 mm). See also
 432 Wang et al. (2016).

433 In addition to changes in peak decoding location, there were differences between
 434 movement and force in their respective overall decoding map patterns (Figure 3). The
 435 between-mode distance D_{inter} , which measured differences between the movement-force
 436 maps (see Methods), was significantly greater than the within-mode distance D_{intra} in 6 of
 437 7 subjects ($p < 3 \times 10^{-5}$ except S3, where $p = 0.19$; one-tailed Wilcoxon signed-rank test with
 438 Bonferroni correction for multiple comparisons; see Figure 3B). This indicates that the
 439 spatial distribution of decoding as a whole changed significantly between movement and

440 force, and that this change was greater than what would be expected from behavioral
 441 variation. Taken together, these results indicate that the spatial representations of
 442 movement and force on the cortical surface are different.

443

444 **Differences in pre-movement, movement, and force behavioral modes were reflected**
 445 **in a dynamical systems model of M1/PM network activity**

446 We next examined the activity of the recorded cortical network as a whole during
 447 the movement-force behavior. The preceding spectral/spatial analyses (Figure 2 and 3)
 448 treated individual ECoG electrodes as independent sources of information. Here, we
 449 instead sought a low-dimensional representation to clarify and summarize the activity of
 450 the cortical network during the time course of the behavior. We used latent factor
 451 analysis via dynamical systems (LFADS; Pandarinath et al., 2018) to generate low-
 452 dimensional representations of single-trial activity in the ECoG feature state space (see
 453 Methods). To visually summarize the factors, we computed principal components of the
 454 LFADS-denoised ECoG features (labeled LFADS-PCs). Figure 4 shows the underlying
 455 dynamics for S5 and S6 during trials of the kinematic-kinetic task, color-coded by
 456 behavioral mode. At the start of the task (pre-movement), the high- and low-frequency
 457 latent factors tended to be distributed through a relatively broad region of the state space
 458 (ex. Figure 4A, red). Prior to the start of movement, the latent factors tended to converge
 459 onto a smaller region of state space, and their trajectories through the movement (cyan)
 460 and force (blue) periods of the task were more tightly grouped. Moreover, each time
 461 period of the task occupied a different part of state space (note the grouping of colors in
 462 Figure 4). To illustrate the impact of LFADS in revealing well-ordered, low dimensional

state space representations, we also performed PCA directly on the ECoG features (PCA-only; Figure 4, inset boxes). In some cases, PCA-only resulted in a rough grouping of behavioral modes (pre-movement, movement, and force) in neural state space (ex. Figure 4A). However, the individual PCA-only trial trajectories remained highly variable, unlike the highly repeatable LFADS-PC trajectories. In other cases, PCA-only did not allow us to resolve a low-dimensional state space representation with identifiable groupings at all (ex. Figure 4D). Contrasting the LFADS-PC plots with the PCA-only plots (i.e., comparing each panel of Figure 4 with its inset) illustrates the benefit of LFADS in visualizing this dataset. We quantified this benefit in Table 2, which shows the number of components required to account for 90% of the variance in the data, with and without LFADS.

474

	PCA-only	LFADS PCs
S01	43 / 66	2 / 66
S02	32 / 48	2 / 48
S03	26 / 44	2 / 44
S04	24 / 32	3 / 32
S05	40 / 74	3 / 74
S06	35 / 72	2 / 72
S07	19 / 36	2 / 36
S08	24 / 40	2 / 40
S09	28 / 38	4 / 38
S10	27 / 36	3 / 36

S11	27 / 36	3 / 36
S12	32 / 78	2 / 78

Table 2. Number of principal components (PCs) required to account for 90% of the variance in the ECoG features (PCA-only) or the latent factors (LFADS PCs).

A neural vector angle summarizes temporal changes across the feature space

Visualizing the low-dimensional state space with LFADS-PCs reinforced the idea that pre-movement, movement, and force behavioral modes are well-represented in neural state space. However, those methods did not allow us to generalize across subjects. Therefore, we used a second metric for summarizing the modulations of feature space across trials and subjects: the NVA. The NVA $\theta(t)$ is the angle at time t between a neural vector $\mathbf{m}(t)$ and its reference direction, \mathbf{m}^{ref} (see Methods). Here, the high-dimensional vector $\mathbf{m}(t)$ was comprised of M1/PM ECoG spectral features. The reference vector \mathbf{m}^{ref} was calculated during a window prior to the moment of peak force in each trial. Therefore $\theta(t)$ measures the dissimilarity between the ECoG features at each moment with their values during peak force generation.

To maximize the signal-to-noise ratio of $\theta(t)$, the elements of $\mathbf{m}(t)$ were selected using a cluster analysis (see Methods). The resulting clusters were typically (1) a cluster of well-modulated low-frequency features (ex. Figure 5A), (2) a cluster of well-modulated high-frequency features (ex. Figure 5B), and (3) a cluster of poorly modulated features (not shown). We computed $\theta(t)$ separately for clusters (1) and (2) in each subject (Figure 5C,D). The NVA recasts feature modulations for each trial into a common unit (angular difference in degrees). Therefore, we were able to combine NVA

496 results across all trials in all subjects, yielding a compact study-wide representation of the
 497 cortical response to the movement-force transition (Figure 5E,F).

498 Across subjects, average low-frequency NVAs began to decrease immediately
 499 after the presentation of the cue to start the trial (Figure 5E, red line), and reached their
 500 minimum value approximately at the start of flexion (Figure 5E, cyan line). Accordingly,
 501 low-frequency NVA during movement was significantly lower than NVA during the pre-
 502 movement period ($p < 10^{-9}$; Kruskal-Wallis test, Tukey HSD post-hoc for all statistical
 503 comparisons in this section). By contrast, there was no significant difference between the
 504 movement period and force ($t=0$ to $t=0.75$) in the low-frequency NVAs ($p=0.32$). High-
 505 frequency NVAs did not deviate from their pre-movement values at target presentation
 506 (Figure 5F), instead changing just prior to the start of movement (Figure 5F, cyan line).
 507 During movement, high-frequency NVAs were significantly higher than pre-movement
 508 NVA ($p < 10^{-9}$), peaking just before the onset of force (Figure 5F, approximately $t = -130$
 509 ms relative to force onset). During the force behavioral mode, high-frequency NVA were
 510 overall lower than either movement ($p < 10^{-9}$) or pre-movement ($p < 10^{-6}$) periods.

511 Overall, the NVA provided a compact way to summarize cortical state space
 512 changes across subjects during the sequential movement-force task. Earlier, Figure 2
 513 showed that responses of individual ECoG features could be quite heterogeneous in their
 514 modulations to behavioral events. Here, Figure 4 and Figure 5 showed that in spite of
 515 that heterogeneity of individual feature modulations, the information conveyed by
 516 populations of features exhibited repeatable, statistically significant patterns during these
 517 behaviors. Like Figure 2, the NVA results suggest the possibility of different cortical
 518 responses by particular parts of the frequency spectrum (low- and high-frequency

519 features). However, the NVA suggests that, while there may be exceptions (as seen in
520 Fig. 2), this distinction may be a general characteristic of M1/PM cortices during the
521 movement-force behavior.

522

523 **ECoG features enabled accurate classification of behavioral modes**

524 Accurately decoding behavioral modes during grasp has potential applications for
525 brain-machine interface (BMI) design. For example, in response to evolving functional
526 goals (e.g., changing from movement to force behavior when picking up an object), a
527 BMI could switch control strategies. To estimate the accuracy such control might
528 achieve, we tested whether the subjects' behavioral modes could be decoded from
529 cortical activity. We used the low- and high-frequency ECoG spectral features to classify
530 each time bin as one of three behavioral modes: pre-movement, movement, or force
531 execution. The ground-truth behavior mode distinctions were labelled according to the
532 movement onset and force onset events (see Figure 1B for an example trial). In parallel
533 with the ECoG feature-based classification, we also classified behavioral mode using the
534 LFADS-denoised features as inputs. This gave us a way to estimate the impact of
535 cortical "noise" on the accuracy of decoding behavioral mode. We used two widely
536 available classifiers: support vector machines (SVM) and boosted aggregate (bagged)
537 decision trees. For each subject, we also calculated a chance decoding value (see
538 Methods). We report classification accuracy for the two types of classifiers separately,
539 evaluating both the features and the LFADS-denoised factors. The three behavioral
540 modes were strongly differentiable in all subjects (Figure 6). Overall, the tree-based
541 classifier outperformed SVM, and LFADS-denoised features were decoded more

eNeuro Accepted Manuscript

542 accurately than the features without denoising ($p=1.9^{-7}$, Kruskal-Wallis test). For the
543 tree-based classifier of LFADS-denoised features, median decoding accuracies for the
544 subjects ranged from $87\%\pm 2\%$ to $94\%\pm 1\%$, with an overall median value of $90\%\pm 6\%$,
545 indicating that these three classes were highly separable. Statistically, the decoding
546 accuracy for all subjects was significantly higher than chance. We emphasize here that
547 each 25 ms time bin was decoded, rather than decoding behavioral modes as blocks of
548 time. Thus, these behavioral modes have separable cortical representations on a 25-ms
549 time scale.

550

551 **Discussion**

552 Manipulating objects dexterously requires controlling both grasp kinematics and
553 isometric force. Even simple activities like turning a doorknob, shaking hands, and
554 lifting a cup of liquid could not be accomplished safely and quickly without both kinds of
555 control. More than two decades ago, investigators began to appreciate that the central
556 nervous system may handle these two vital aspects of motor behavior separately
557 (Flanagan et al., 1999). Here, we found quantifiable differences in how the motor and
558 premotor cortices represented behavioral mode, i.e. pre-movement, flexion movement,
559 and isometric force. We found individual feature modulations that were time-locked to
560 behaviorally relevant events, and could be observed on a single-trial basis (Figure 2). As
561 ensembles, the ECoG modulations constituted a neural state change, accompanying
562 changes in behavioral mode. We were able to model this change using a dynamical
563 systems approach (LFADS), and decode the subjects' behavioral modes with high

564 accuracy. Understanding neural state changes like these in the context of a functional
 565 grasp task will inform the design of dexterous grasp brain-machine interfaces.

566 Generally, we achieved highly accurate decoding of the continuous time course of
 567 the behavioral variables (movement and force). These results compared favorably with
 568 prior studies decoding finger movement kinematics (Acharya et al., 2010; Nakanishi et
 569 al., 2014; Xie et al., 2018) and isometric force (Pistohl et al., 2013; Chen et al., 2014;
 570 Flint et al., 2014; Vaidya et al., 2019). Importantly, there was no significant difference in
 571 our ability to decode force and movement across subjects, implying that any differences
 572 in cortical representations of force and movement were not simply expressions of a
 573 superior decoding of one or the other.

574 Spatially, human cortical encoding of finger movement takes place over a
 575 widespread area (Schieber, 2002), including complex and overlapping representations of
 576 individual finger movements (Dechent and Frahm, 2003). ECoG recordings make it
 577 possible to examine cortical activity on these relatively large spatial scales (Slutzky and
 578 Flint, 2017). We found that the maps of decoding performance altered significantly
 579 across movement and force representations (across-mode) in 6 of 7 subjects. We
 580 controlled for changes due to time or behavioral variability (within-mode), by comparing
 581 the between-mode maps to the within-mode maps. One potential explanation for the
 582 spatial map differences could be that the activating regions of the maps are simply
 583 shrinking during isometric force. Such an explanation is consistent with evidence
 584 pointing to less cortical modulation with isometric force than with movement (Hendrix et
 585 al., 2009). However, in this case we found that the peaks of the decoding maps changed
 586 location (Table 1), indicating that the maps shifted rather than merely growing or

shrinking. These spatial decoding results are relevant to the design of brain-machine interfaces (BMIs), since any BMI that restores grasp should ideally execute both movement and force functions. There is evidence that representations of hand movements are preserved following amputation (Bruurmijn et al., 2017), though it remains to be shown whether the movement-force functional map change will remain in an individual with paralysis. Downey et al. (2017) found that applying a scaling factor to neuronal spike rates facilitated the ability of human BMI users to grasp objects with a prosthetic hand. The utility of such a scaling factor may be a reflection of the functional somatotopy of the cortex, though the current results suggest that amplitude scaling would not necessarily be the ideal method of accounting for the difference in movement and force representations. Here, we found the mean shift in peak decoding location was 9.9 mm, a sizeable distance in the cerebral cortex. The overall differences in spatial decoding maps (patterns of decoding), while significant, were not large. However, this was not unexpected for two related motor activities (movement and force, in the context of a grasp-like behavior) performed by the same finger.

Increasingly, spiking activity in small areas of motor cortex has been modeled as a dynamical system in an effort to parsimoniously describe and understand network-level neuronal activity. In this study, we used LFADS to uncover low-dimensional neural state spaces for each subject. LFADS-PCs were tightly grouped over trials and occupied distinct regions of state space during the pre-movement, movement, and force behavioral modes (Figure 4). Both low-frequency and high-frequency LFADS-PCs were clearly separated in different behavioral modes. Some previous examples of modeling cortical dynamics using latent factors have analyzed single behavioral modes. For example,

Vaidya et al. (2015) modeled both reach- and grasp-related neural ensembles as linear dynamical systems to study learning. Also, Gallego et al. (2018) also showed that there were some differences in local M1 neuronal ensemble activity between kinematic and kinetic cursor control tasks. Our results show that dynamical systems modeling can elucidate the latent factors underlying a widespread cortical network in addition to local circuit networks. It was not surprising that latent factor state space trajectories evolved with time during each trial; indeed, this is a fundamental underlying assumption of the dynamical systems model. The significance of the LFADS-derived trajectories was their smooth, repeatable paths through distinct regions of state space during behavioral mode transitions. Compared with PCA-only state space trajectories, LFADS factors clustered more tightly and evolved much more repeatably in pre-movement, movement, and force behavioral modes.

We used the NVA to summarize spectro-temporal changes across electrodes and subjects. The average duration of high-frequency neural vector changes (about 300 ms; Figure 5F) was substantially shorter than the average duration of the force-matching part of the behavioral task (about 1 s). A phasic rise in high gamma modulation near the onset of behavior has been shown during other grasp force behaviors (Chen et al., 2014; Branco et al., 2019b), as well as isotonic movement (Flint et al., 2017). Single-neuron studies in nonhuman primates also support the phasic modulation with force onset (Hendrix et al., 2009), or more often, phasic-tonic modulation (Maier et al., 1993; Mason et al., 2002; Intveld et al., 2018). This agreement makes sense when considering that high-gamma activity is often correlated with ensemble spiking. It appears that the onset of force

632 behavior, or perhaps the transition from movement to force, is especially meaningful to
633 the cortex when encoding grasp.

634 Our results support and extend the findings of Venkadesan and Valero-Cuevas
635 (2008), who inferred from muscle activity that the human motor system uses two separate
636 control strategies for movement and isometric force. Importantly, they observed muscle
637 activity changing about 100 ms prior to force onset, ruling out the conclusion that
638 changes in EMG patterns are purely the result of the mechanical constraints of the
639 behavior. In the current study, we chose \mathbf{m}^{ref} in part to facilitate comparison with that
640 study. We found similarities between the cortical low-frequency NVA and their angular
641 deviation for muscle coordination patterns (Figure 2A from that study), though our low-
642 frequency NVAs changed earlier: approximately 350 ms prior to force onset, which is
643 compatible with the delay between cortical and muscular activity. Changes in high
644 gamma activity patterns (reflected by the NVA), on the other hand, occurred around 130
645 ms prior to force onset. This time course of changing cortical activity is consistent with
646 the earlier EMG results, and with the concept that control strategies for movement and
647 force are encoded in the motor and premotor cortices, rather than subcortical systems.
648 This argues against the hypothesis that differences in cortical activity during movement-
649 force are due mainly to somatosensory feedback changes in the two states.

650 We believe the present data indicate that the cortical state-spaces are different
651 among pre-movement, movement, and force. One possible hypothesis to explain this
652 difference is that additional muscles (other than index finger flexors) may have been
653 recruited during force mode compared to movement mode, for example to additionally
654 stabilize the wrist. While we were not able to include EMG recordings because of time

655 and access limitations to our participants, recording EMG simultaneously with ECoG
 656 might allow us to test such a hypothesis. However, Venkadesan and Valero-Cuevas
 657 (2008), who recorded EMG (but not neural activity) in a similar task, found that neural
 658 control strategies changed within the scope of finger flexor muscles: that is, the same
 659 muscles were used in different recruitment patterns. Overall, these findings are also
 660 consistent with prior work showing that M1 neurons display muscle-like encoding (Oby
 661 et al., 2013).

662 We note that our behavioral task was chosen to recreate a naturalistic movement-
 663 force model of object grasp, and was not designed to systematically explore the finger-
 664 movement kinematic-kinetic space. Specifically, we note the caveat that movement
 665 behavior was not required to be as variable as force, since no explicit movement “targets”
 666 were designated (unlike force targets which varied randomly). Accordingly, we designed
 667 the analysis of spatial decoding map differences (Figure 3) in such a way as to control for
 668 within-mode variation over time. In addition, we observed much larger differences
 669 between movement and force behavioral modes than within mode, in both the latent
 670 factor trajectories (Figure 4) and in our statistical analysis of the NVA values (Figure 5).
 671 Thus, the data still support distinct cortical modes that correspond to distinct behavioral
 672 modes.

673 Our decoding of the subjects’ time-varying behavioral mode has ramifications for
 674 BMI design, as demonstrated by Suminski et al. (2013). Suminski et al. addressed a
 675 longstanding limitation of BMIs: decoders trained on a given set of motor activities do
 676 not predict accurately outside those activities. Hierarchical BMIs, which include multiple
 677 decoders operating in parallel with a switching mechanism, may outperform those with a

678 single decoder. In the context of hand function, a decoder trained only on movement data
679 may not provide optimal control of a BMI for grasping and manipulating objects, either
680 with a prosthetic hand or functional electrical stimulation of paralyzed fingers. The most
681 important challenge for current BMI design is to bring this technology more fully into the
682 clinic. Thus, practical considerations, like understanding the differences in the neural
683 representations of imagined and attempted movement (Vargas-Irwin et al., 2018) or force
684 (Rastogi et al., 2020) by an individual with paralysis, are high priorities. In a similar
685 vein, our results—suggesting that decoding the behavioral kinematic/kinetic mode from
686 cortical activity is feasible—could increase the functionality of BMIs during object grasp.
687 In addition, the improvement in behavioral mode decoding by using latent factors
688 indicates that viewing the cortical motor control circuits as a dynamical system can
689 facilitate the task of identifying cortical correlates of multiple behavioral modes. LFADS
690 does not add information to that contained in the ECoG features, so its application may
691 not always result in a large increase in decoding accuracy (especially in a discrete
692 classification task, e.g., Figure 6, S6), despite its effectiveness at uncovering low-
693 dimensional representations (Figure 4B,D, also from S6). However, the success of
694 LFADS in improving decoding in some subjects, especially those with worse initial
695 performance, suggests a potentially important role for denoising procedures such as
696 LFADS in BMI future BMI applications. Improving decoding accuracy of behavioral
697 mode from 77% to 91%, as in S4 (Figure 6), would likely result in greatly improved
698 overall BMI performance, more positive perceptions by the user, and better acceptance of
699 the prosthesis.

700 The ubiquity of object-manipulation behaviors in human life underscores the
701 importance of functioning hand grasp. In this case, however, ubiquity does not mean that
702 the behavior is simple. The current study allowed us to examine the activity in human
703 M1/PM that accompanied the sequential execution of movement and force. We found
704 both movement and force to be quite well represented, allowing us to decode each with
705 high accuracy. Our data also indicate that the movement and force representations are
706 distinct, as we distinguished them in space, with LFADS, via the Neural Vector Angle,
707 and via behavioral mode classification. The current results suggest that a BMI controlled
708 using ECoG could restore both movement and isometric aspects of grasp to individuals
709 with paralysis.
710

711 **References**

- 712 Acharya S, Fifer MS, Benz HL, Crone NE, Thakor NV (2010) Electrographic
 713 amplitude predicts finger positions during slow grasping motions of the
 714 hand. *J Neural Eng* 7:046002.
- 715 Ajiboye AB, Willett FR, Young DR, Memberg WD, Murphy BA, Miller JP, Walter BL,
 716 Sweet JA, Hoyen HA, Keith MW, Peckham PH, Simeral JD, Donoghue JP,
 717 Hochberg LR, Kirsch RF (2017) Restoration of reaching and grasping
 718 movements through brain-controlled muscle stimulation in a person with
 719 tetraplegia: a proof-of-concept demonstration. *Lancet* 389:1821-1830.
- 720 Blabe CH, Gilja V, Chestek CA, Shenoy KV, Anderson KD, Henderson JM (2015)
 721 Assessment of brain-machine interfaces from the perspective of people with
 722 paralysis. *J Neural Eng* 12:043002.
- 723 Bouton CE, Shaikhouni A, Annetta NV, Bockbrader MA, Friedenberg DA, Nielson DM,
 724 Sharma G, Sederberg PB, Glenn BC, Mysiw WJ, Morgan AG, Deogaonkar M,
 725 Rezai AR (2016) Restoring cortical control of functional movement in a
 726 human with quadriplegia. *Nature* 533:247-250.
- 727 Branco MP, de Boer LM, Ramsey NF, Vansteensel MJ (2019a) Encoding of kinetic and
 728 kinematic movement parameters in the sensorimotor cortex: A Brain-
 729 Computer Interface perspective. *Eur J Neurosci*.
- 730 Branco MP, Geukes SH, Aarnoutse EJ, Vansteensel MJ, Freudenburg ZV, Ramsey NF
 731 (2019b) High-frequency band temporal dynamics in response to a grasp
 732 force task. *J Neural Eng* 16:056009.

- 733 Bruurmijn M, Pereboom IPL, Vansteensel MJ, Raemaekers MAH, Ramsey NF (2017)
 734 Preservation of hand movement representation in the sensorimotor areas of
 735 amputees. *Brain* 140:3166-3178.
- 736 Chen C, Shin D, Watanabe H, Nakanishi Y, Kambara H, Yoshimura N, Nambu A, Isa T,
 737 Nishimura Y, Koike Y (2014) Decoding grasp force profile from
 738 electrocorticography signals in non-human primate sensorimotor cortex.
 739 *Neurosci Res* 83:1-7.
- 740 Chib VS, Krutky MA, Lynch KM, Mussa-Ivaldi FA (2009) The separate neural control
 741 of hand movements and contact forces. *J Neurosci* 29:3939-3947.
- 742 Churchland MM, Cunningham JP, Kaufman MT, Foster JD, Nuyujukian P, Ryu SI,
 743 Shenoy KV (2012) Neural population dynamics during reaching. *Nature*
 744 487:51-56.
- 745 Collard MJ, Fifer MS, Benz HL, McMullen DP, Wang Y, Milsap GW, Korzeniewska A,
 746 Crone NE (2016) Cortical subnetwork dynamics during human language
 747 tasks. *Neuroimage* 135:261-272.
- 748 Danion F, Diamond JS, Flanagan JR (2013) Separate contributions of kinematic and
 749 kinetic errors to trajectory and grip force adaptation when transporting
 750 novel hand-held loads. *J Neurosci* 33:2229-2236.
- 751 Dechent P, Frahm J (2003) Functional somatotopy of finger representations in
 752 human primary motor cortex. *Hum Brain Mapp* 18:272-283.
- 753 Downey JE, Brane L, Gaunt RA, Tyler-Kabara EC, Boninger ML, Collinger JL (2017)
 754 Motor cortical activity changes during neuroprosthetic-controlled object
 755 interaction. *Sci Rep* 7:16947.

- 756 Downey JE, Weiss JM, Flesher SN, Thumser ZC, Marasco PD, Boninger ML, Gaunt RA,
 757 Collinger JL (2018) Implicit Grasp Force Representation in Human Motor
 758 Cortical Recordings. *Front Neurosci* 12:801.
- 759 Evarts EV (1968) Relation of pyramidal tract activity to force exerted during
 760 voluntary movement. *J Neurophysiol* 31:14-27.
- 761 Fagg AH, Ojakangas GW, Miller LE, Hatsopoulos NG (2009) Kinetic trajectory
 762 decoding using motor cortical ensembles. *IEEE Trans Neural Syst Rehabil*
 763 *Eng* 17:487-496.
- 764 Flanagan JR, Nakano E, Imamizu H, Osu R, Yoshioka T, Kawato M (1999)
 765 Composition and decomposition of internal models in motor learning under
 766 altered kinematic and dynamic environments. *J Neurosci* 19:RC34.
- 767 Flint RD, Rosenow JM, Tate MC, Slutzky MW (2017) Continuous decoding of human
 768 grasp kinematics using epidural and subdural signals. *J Neural Eng*
 769 14:016005.
- 770 Flint RD, Wang PT, Wright ZA, King CE, Krucoff MO, Schuele SU, Rosenow JM, Hsu FP,
 771 Liu CY, Lin JJ, Sazgar M, Millett DE, Shaw SJ, Nenadic Z, Do AH, Slutzky MW
 772 (2014) Extracting kinetic information from human motor cortical signals.
 773 *Neuroimage* 101:695-703.
- 774 Gallego JA, Perich MG, Naufel SN, Ethier C, Solla SA, Miller LE (2018) Cortical
 775 population activity within a preserved neural manifold underlies multiple
 776 motor behaviors. *Nat Commun* 9:4233.

- 777 Hendrix CM, Mason CR, Ebner TJ (2009) Signaling of grasp dimension and grasp
778 force in dorsal premotor cortex and primary motor cortex neurons during
779 reach to grasp in the monkey. *J Neurophysiol* 102:132-145.
- 780 Hochberg LR, Bacher D, Jarosiewicz B, Masse NY, Simeral JD, Vogel J, Haddadin S, Liu
781 J, Cash SS, van der Smagt P, Donoghue JP (2012) Reach and grasp by people
782 with tetraplegia using a neurally controlled robotic arm. *Nature* 485:372-
783 375.
- 784 Hotson G, McMullen DP, Fifer MS, Johannes MS, Katyal KD, Para MP, Armiger R,
785 Anderson WS, Thakor NV, Wester BA, Crone NE (2016) Individual finger
786 control of a modular prosthetic limb using high-density electrocorticography
787 in a human subject. *J Neural Eng* 13:026017.
- 788 Hunter IW, Korenberg MJ (1986) The identification of nonlinear biological systems:
789 Wiener and Hammerstein cascade models. *Biol Cybern* 55:135-144.
- 790 Intveld RW, Dann B, Michaels JA, Scherberger H (2018) Neural coding of intended
791 and executed grasp force in macaque areas AIP, F5, and M1. *Sci Rep* 8:17985.
- 792 Maier MA, Bennett KM, Hepp-Reymond MC, Lemon RN (1993) Contribution of the
793 monkey corticomotoneuronal system to the control of force in precision grip.
794 *J Neurophysiol* 69:772-785.
- 795 Mason CR, Gomez JE, Ebner TJ (2002) Primary motor cortex neuronal discharge
796 during reach-to-grasp: controlling the hand as a unit. *Arch Ital Biol* 140:229-
797 236.
- 798 Moran DW, Schwartz AB (1999) Motor cortical representation of speed and
799 direction during reaching. *J Neurophysiol* 82:2676-2692.

- 800 Nakanishi Y, Yanagisawa T, Shin D, Chen C, Kambara H, Yoshimura N, Fukuma R,
801 Kishima H, Hirata M, Koike Y (2014) Decoding fingertip trajectory from
802 electrocorticographic signals in humans. *Neurosci Res* 85:20-27.
- 803 Oby ER, Ethier C, Miller LE (2013) Movement representation in the primary motor
804 cortex and its contribution to generalizable EMG predictions. *J Neurophysiol*
805 109:666-678.
- 806 Pandarinath C, O'Shea DJ, Collins J, Jozefowicz R, Stavisky SD, Kao JC, Trautmann EM,
807 Kaufman MT, Ryu SI, Hochberg LR, Henderson JM, Shenoy KV, Abbott LF,
808 Sussillo D (2018) Inferring single-trial neural population dynamics using
809 sequential auto-encoders. *Nature methods* 15:805-815.
- 810 Pfurtscheller G, Muller GR, Pfurtscheller J, Gerner HJ, Rupp R (2003) 'Thought'--
811 control of functional electrical stimulation to restore hand grasp in a patient
812 with tetraplegia. *Neurosci Lett* 351:33-36.
- 813 Pistohl T, Schmidt TS, Ball T, Schulze-Bonhage A, Aertsen A, Mehring C (2013) Grasp
814 Detection from Human ECoG during Natural Reach-to-Grasp Movements.
815 *PLoS One* 8:e54658.
- 816 Rastogi A, Vargas-Irwin CE, Willett FR, Abreu J, Crowder DC, Murphy BA, Memberg
817 WD, Miller JP, Sweet JA, Walter BL, Cash SS, Rezaii PG, Franco B, Saab J,
818 Stavisky SD, Shenoy KV, Henderson JM, Hochberg LR, Kirsch RF, Ajiboye AB
819 (2020) Neural Representation of Observed, Imagined, and Attempted
820 Grasping Force in Motor Cortex of Individuals with Chronic Tetraplegia. *Sci*
821 *Rep* 10:1429.

- 822 Schalk G, McFarland DJ, Hinterberger T, Birbaumer N, Wolpaw JR (2004) BCI2000: a
 823 general-purpose brain-computer interface (BCI) system. IEEE Trans Biomed
 824 Eng 51:1034-1043.
- 825 Schieber MH (2002) Motor cortex and the distributed anatomy of finger movements.
 826 Adv Exp Med Biol 508:411-416.
- 827 Slutzky MW (2019) Brain-Machine Interfaces: Powerful Tools for Clinical Treatment
 828 and Neuroscientific Investigations. Neuroscientist 25:139-154.
- 829 Slutzky MW, Flint RD, 3rd (2017) Physiological Properties of Brain Machine
 830 Interface Input Signals. J Neurophysiol:jn 00070 02017.
- 831 Suminski AJ, Tkach DC, Fagg AH, Hatsopoulos NG (2010) Incorporating feedback
 832 from multiple sensory modalities enhances brain-machine interface control. J
 833 Neurosci 30:16777-16787.
- 834 Suminski AJ, Fagg AH, Willett FR, Bodenhamer M, Hatsopoulos NG (2013) Online
 835 adaptive decoding of intended movements with a hybrid kinetic and
 836 kinematic brain machine interface. Conf Proc IEEE Eng Med Biol Soc
 837 2013:1583-1586.
- 838 Sussillo D, Jozefowicz R, Abbott L, Pandarinath C (2016) Lfads-latent factor analysis
 839 via dynamical systems. arXiv preprint arXiv:160806315.
- 840 Vaidya M, Kording K, Saleh M, Takahashi K, Hatsopoulos NG (2015) Neural
 841 coordination during reach-to-grasp. J Neurophysiol 114:1827-1836.
- 842 Vaidya M, Flint RD, Wang PT, Barry A, Li Y, Ghassemi M, Tomic G, Yao J, Carmona C,
 843 Mugler EM, Gallick S, Driver S, Brkic N, Ripley D, Liu C, Kamper D, Do AH,
 844 Slutzky MW (2019) Hemicraniectomy in traumatic brain injury: a

845 noninvasive platform to investigate high gamma activity for brain machine
 846 interfaces. IEEE Trans Neural Syst Rehabil Eng.
 847 Vargas-Irwin CE, Feldman JM, King B, Simeral JD, Sorice BL, Oakley EM, Cash SS,
 848 Eskandar EN, Friehs GM, Hochberg LR (2018) Watch, Imagine, Attempt:
 849 Motor cortex single unit activity reveals context-dependent movement
 850 encoding in humans with tetraplegia. Front Hum Neurosci 12:450.
 851 Venkadesan M, Valero-Cuevas FJ (2008) Neural control of motion-to-force
 852 transitions with the fingertip. J Neurosci 28:1366-1373.
 853 Wang PT, King CE, McCrimmon CM, Lin JJ, Sazgar M, Hsu FP, Shaw SJ, Millet DE, Chui
 854 LA, Liu CY, Do AH, Nenadic Z (2016) Comparison of decoding resolution of
 855 standard and high-density electrocorticogram electrodes. J Neural Eng
 856 13:026016.
 857 Wodlinger B, Downey JE, Tyler-Kabara EC, Schwartz AB, Boninger ML, Collinger JL
 858 (2014) Ten-dimensional anthropomorphic arm control in a human brain-
 859 machine interface: difficulties, solutions, and limitations. J Neural Eng
 860 12:016011.
 861 Xie Z, Schwartz O, Prasad A (2018) Decoding of finger trajectory from ECoG using
 862 deep learning. J Neural Eng 15:036009.
 863 Yanagisawa T, Hirata M, Saitoh Y, Kishima H, Matsushita K, Goto T, Fukuma R, Yokoi
 864 H, Kamitani Y, Yoshimine T (2012) Electrocorticographic control of a
 865 prosthetic arm in paralyzed patients. Annals of neurology 71:353-361.
 866
 867

868 **Figure/Table legends**

869

870 Figure 1. ECoG array placement, experimental task, and behavioral data. (A) In S1 through S5
871 and S7, we targeted the primary motor and premotor cortices. Array placement for S6 was
872 determined by clinical need. For S1 and S2 we recorded ECoG from the right hemisphere; the
873 other subjects' ECoG were recorded from the left hemisphere. (B) One trial (approximately 2.5s)
874 of the kinematic-kinetic task. At the beginning of the trial, the subjects held their index finger in
875 a neutral position (upper left photograph) until visually cued on a screen. Cyan trace: finger
876 kinematics (amount of flexion; arbitrary units) during the trial. Cyan triangle: time of flexion
877 movement onset. Upon contact with the force sensor (lower inset photograph), the subjects
878 exerted isometric force until matching a force target on the screen with a cursor (not shown).
879 Blue trace: recorded force. Blue circle: time of force onset. At bottom is a schematic
880 representation of behavioral mode segmentation: pre-movement (from target presentation until
881 the start of flexion), movement (start of flexion until start of force), and force (from force onset
882 lasting 500ms). (C) We measured index finger flexion using a CyberGlove; movement onset was
883 identified using the first principal component calculated on the data from the highlighted sensors.

884

885

886 Figure 2. Spectral power modulation during the movement-force grasp task. Each panel shows
887 data from a high- or low-frequency spectral feature taken from an individual ECoG electrode.
888 The single-trial frequency band power (grayscale in each plot) was z-scored and aligned either to
889 movement onset (cyan dashed lines, **A-C,F**) or to force onset (blue dashed lines, **D-E**). Blue
890 circles show force onset times when trials were aligned to movement onset. Cyan triangles show
891 movement onset times when trials were aligned to force onset. High frequency features (**A-C**)
892 exhibited power increases, which could be time locked to both movement and force (**A**) or force
893 only (**B,C**). Low frequency features (**D-F**) exhibited power decreases just preceding, and aligned
894 to, the onset of movement (**D,E**), or aligned to the start of force (**F**).

Figure 3. Decoding maps reveal changes in the cortical representations of movement and force. (A) Example decoding maps for S4. Four folds of data are shown, the actual analysis utilized 10 folds per recording. Square recording arrays are shown in a rotated perspective for compact visualization. We compared single-electrode decoding maps for movement (top) and force (bottom) using a distance metric D_{inter} for every possible combination of fold pairs. As a control, we calculated D_{intra} between all possible fold pairs, for within-movement and within-force decoding. (B) Boxplot of distance measures for all subjects. The central horizontal line in each box shows the median, while the notches show 95% confidence intervals. Overall, the median D_{inter} was significantly greater than the median D_{intra} in 6 of 7 subjects (red stars). Note that the maps in (A) show 64 channels; for the distance measures in (B), only the PM/M1 electrodes were included.

Figure 4. Modeling ECoG features as an underlying dynamical system using LFADS uncovers repeatable trajectories through a low-dimensional state space during the kinematic-kinetic task. Shown are LFADS-PCs (labeled as “PC” for simplicity) derived from high-frequency (A-B) and low-frequency (C-D) ECoG features. Single-trial trajectories are shown for subjects S5 (78 trials; panel A,C) and S6 (73 trials; panel B,D). Inset boxes in each panel show the trajectories resulting from PCA performed directly on the ECoG features (without LFADS). The color code at bottom defines the portion of each trial corresponding to each behavioral mode.

Figure 5. The neural vector angle (NVA) summarizes the cortical state change associated with the behavioral mode change from movement to force. (A,B) Electrodes selected for S5, using k-means clustering. CS; central sulcus. Anterior-posterior and superior-inferior are indicated on the rosette; compare to Figure 1A. (A) and (B) represent two of the three resulting clusters; the unsupervised cluster analysis natively divided the responses into low frequency and high frequency responses. (C) The NVA, $\theta(t)$ for the low frequency features selected in (A). The dark

921 red dashed line shows the average time of target appearance, relative to force onset (time=0). The
 922 vertical cyan lines show the mean (solid line) and standard deviation (dashed lines) of movement
 923 onset, relative to force onset. The vertical black lines show the time of maximum force for each
 924 trial (equivalent to the reference period \mathbf{m}^{ref}). **(D)** The NVA for the high frequency features
 925 shown in **(B)**. **(E,F)** NVAs calculated across all trials, all subjects in the study. Labeling
 926 conventions are the same as in **(C,D)**.

927

928 Figure 6. Decoding behavioral mode from ECoG features before and after LFADS denoising.
 929 The median classification accuracy was greater than chance for all subjects. SVM; support vector
 930 machines. Tree; boosted aggregate decision tree classifier.

931

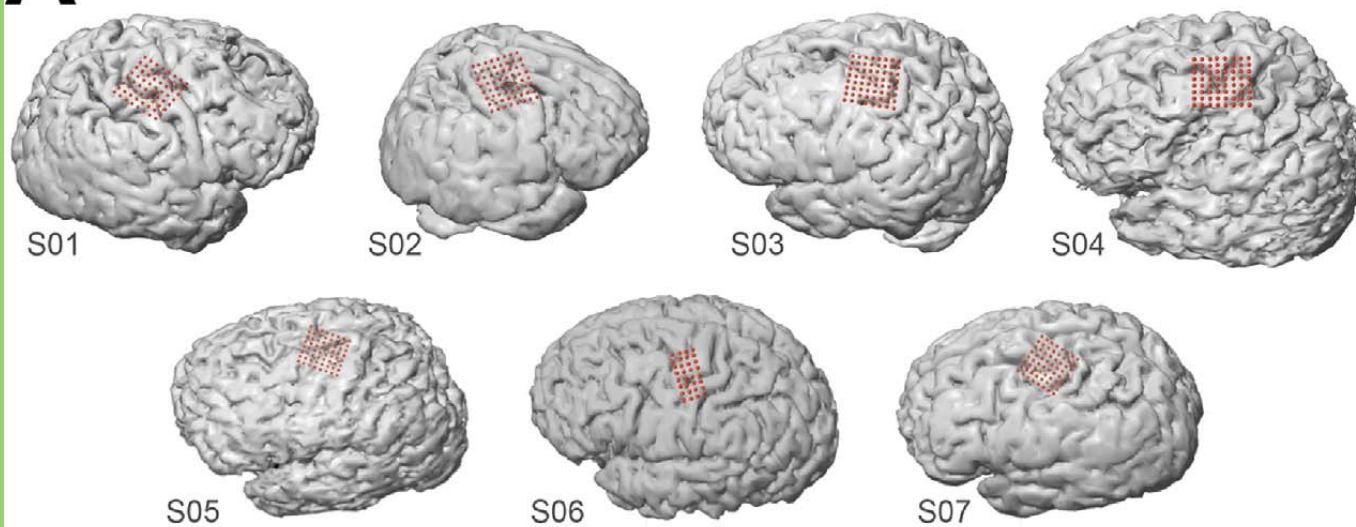
932 Table 1. Displacement of peak location for movement decoding performance relative to force
 933 decoding performance in each subject.

934

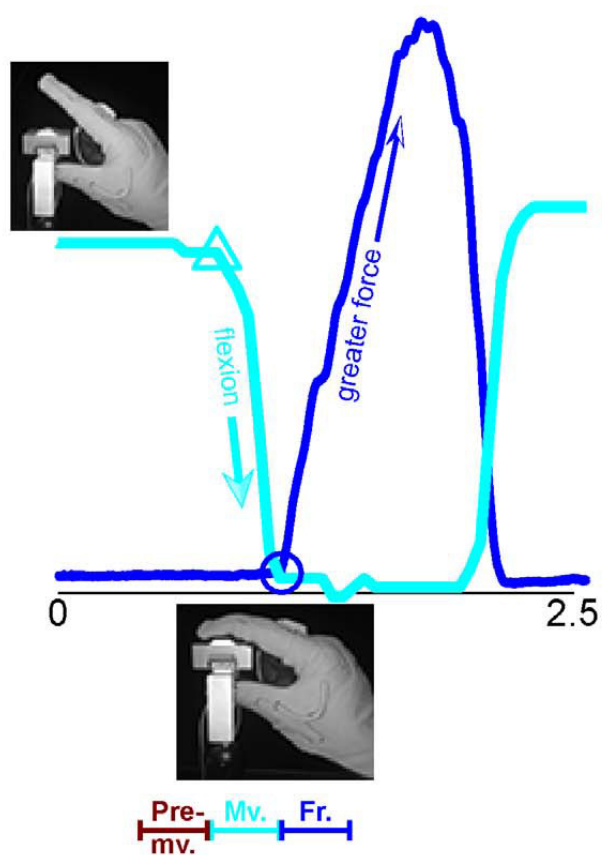
935 Table 2. Number of principal components (PCs) required to account for 90% of the variance in
 936 the ECoG features (PCA-only) or the latent factors (LFADS PCs). Note that the number of
 937 available features (factors) was equal to twice the number of ECoG electrodes selected for the
 938 analysis (those in M1/PM areas).

939

A



B



C



